Acta Materialia 208 (2021) 116730

Contents lists available at ScienceDirect

Acta Materialia

journal homepage: www.elsevier.com/locate/actamat

Large-deformation plasticity and fracture behavior of pure lithium under various stress states

Tobias Sedlatschek[a,b], Junhe Lian[a,c], Wei Li[a], Menglei Jiang[d], Tomasz Wierzbicki[a], Martin Z. Bazant[e,f], Juner Zhu[a,e,*]

[a] Department of Mechanical Engineering, Massachusetts Institute of Technology, 77 Massachusetts Avenue, Cambridge, Massachusetts, 02139, USA
[b] Faculty of Mechanical Engineering, RWTH Aachen University, 52056 Aachen, Germany
[c] Advanced Manufacturing and Materials, Department of Mechanical Engineering, Aalto University, Puumiehenkuja 3, 02150 Espoo, Finland
[d] Department of Materials Science and Engineering, Massachusetts Institute of Technology, 77 Massachusetts Avenue, Cambridge, Massachusetts, 02139, USA
[e] Department of Chemical Engineering, Massachusetts Institute of Technology, 77 Massachusetts Avenue, Cambridge,Massachusetts, 02139, USA
[f] Department of Mathematics, Massachusetts Institute of Technology, 77 Massachusetts Avenue, Cambridge, Massachusetts, 02139, USA

ARTICLE INFO

Article history:
Received 30 October 2020
Revised 6 January 2021
Accepted 5 February 2021
Available online 11 February 2021

Keywords:
Pure lithium
Lithium-metal battery
Mechanical properties
Microstructure
Plasticity
Fracture

ABSTRACT

Although lithium-metal anodes are being extensively examined in research projects aiming at pushing the energy density of lithium batteries to its limit, the knowledge about the mechanical properties of pure lithium is insufficient in two aspects. First, most of the available data focuses either on nano- and micro-scale single-crystalline lithium or on macro-scale bulk material. Second, those tests were commonly performed via uniaxial tests in which the stress states were simple or nanoindentation. This work aims at bridging these gaps by performing a systematic experimental program under various stress states on small-sized specimens and by developing a plasticity model that can capture the important characteristics. Based on these experimental and computational findings, the added value on the understanding of the deformation and failure mechanisms of lithium under various stress states and a first quantitative description on the plasticity anisotropy on lithium is provided. In order to manufacture the required complex-shaped specimens for the five different stress states (uniaxial tension, notched tension with two different radii, central hole tension, and simple shear), a method which allows safe laser cutting of thick lithium foil in argon atmosphere is developed. The tensile tests are conducted in pure argon as well as in air to quantify the effect of oxidation on the strength of lithium. By means of post-mortem microstructural examinations, two active slip systems and cross-slip are observed. Lithium fractures in a perfectly ductile manner when the specimen thickness is reduced to zero due to localized necking. Digital image correlation analysis shows that the lithium foil is highly anisotropic in the through-thickness direction although it is in-plane isotropic. By using a rate-dependent transverse isotropic model, a satisfactory prediction of the five experiments is provided.

1. Introduction

Since lithium-ion batteries are close to reaching the theoretical limit of their energy density, next-generation batteries are currently under development [1]. Replacing the porous graphite anode with pure lithium is a promising approach to increase the amount of energy that can be stored in a battery. An additional advantage is the possibility to integrate the lithium-metal anode into all-solid-state energy storage systems without the otherwise necessary highly flammable liquid electrolyte. By the use of these all-solid-state batteries (ASSBs), the battery safety is improved, for example in electric vehicle crash scenarios [2].

However, the development of a long-living lithium-metal battery is still a continued process. Existing prototype batteries using lithium-metal anodes suffer from the relatively low cycle life and durability (around 400 cycles compared with the over 1200 cycles of commercial lithium-ion cells in the market). One of the important issues is the formation and growth of dendrites during the service life of the battery cell [3]. Lithium dendrites can penetrate into the separator and potentially cause an electrical short

---

[*] Corresponding author.

E-mail addresses: tose@mit.edu (T. Sedlatschek), lianjh@mit.edu (J. Lian), weili17@mit.edu (W. Li), mengleij@mit.edu (M. Jiang), wierz@mit.edu (T. Wierzbicki), bazant@mit.edu (M.Z. Bazant), zhujuner@mit.edu (J. Zhu).

https://doi.org/10.1016/j.actamat.2021.116730

circuit and the failure of the cell [4]. Several recent experimental and theoretical studies that successfully stabilized the cycling performance of liquid-electrolyte lithium-metal batteries showed that inducing mechanical pressure and plastic flow of the lithium is beneficial to suppressing the dendrite formation [5] and breaking lithium whiskers [6,7]. For lithium-metal ASSBs, one essential issue hindering their commercialization is the loss of contact at the interface between the solid electrolyte and the lithium foil [8]. Like the case of liquid-electrolyte lithium-metal cells, many existing studies in the open literature showed that applying an external mechanical pressure on the battery could help to address this issue, thus increasing the cycle performance by two to three folds [9–11].

While various models have been developed, the underlying physics of the pressure effect is still not fully understood. One of the obstacles is the lack of a reliable mechanical characterization of pure lithium. Monroe and Newman [12] proposed perhaps the first electrochemical model of a solid-state lithium-metal battery that considered the pressure effect on the thermodynamics and kinetics, but their model assumed linear elasticity of pure lithium, which is not realistic. Barai et al.[13] extended this model by introducing an elasto-plasticity theory to describe the mechanical deformation of pure lithium. Recently, Zhang et al. [14,15] developed a model of the lithium – solid electrolyte interface by considering the roughness of the two components. The authors reported that even under a low external pressure of 700 kPa, the lithium foil can locally reach the yielding criterion and develop a large plastic deformation due to the localization caused by the surface roughness. This finding emphasizes the importance of an accurate plasticity model of pure lithium. Anand and Narayan [16,17] developed an elastic-viscoplastic model for lithium and applied it to model the large deformation during the formation of lithium dendrites. Even calibrated with a limited amount of data from the open literature, this model showed promise for battery characterization.

One fundamental challenge of investigating the mechanical properties of pure lithium stems from its size effect. An overview can be found in two recent articles [18,19]. The general trend is that small-scale dendrites are significantly stronger then large-scale bulk lithium, which is not new to the mechanics community who have seen the same trend in other materials [20]. Existing data that has been reported in the open literature focuses either on micro-scale single crystalline lithium [21] or on macro-scale bulk material [18,22–25]. Two recent studies [18,26] successfully obtained the mechanical properties of lithium at nano-scale by growing whiskers and using an atomic force microscope (AFM) to apply compressive forces. Even with these important progresses, there is still a clear gap in the existing research, which is the meso-scale – that is a specimen size that ranges from several micrometers to about one millimeter – which corresponds to the thickness of a lithium-metal anode. To the best knowledge of the authors, only two studies have investigated this range. Fincher et al. [19] carried out nanoindentation and tensile tests on a 150 μm-thick pure lithium foil. Although the size of the tested lithium samples was still at the macro-scale, the indentation depth and the plastic deformation zone were around 10 μm, falling in the meso-scale range. Herbert et al. [27] performed nanoindentation tests on 5 and 18 μm-thick pure lithium films to measure the elastic modulus.

Another limitation of the available experimental data on pure lithium is that the investigated stress states were relatively simple and usually did not cover large deformation to fracture. As a result, most of the existing studies were focused on the basic linear elasticity and uniaxial plasticity parameters. Much work was done on the description of the elastic properties of lithium including the Young's modulus and the yield stress. The Young's modulus was measured in mechanical tests including uniaxial tensile tests [22], compression or upsetting tests [18,23], bending [24], nano-indentation [19,27,28] and flat punch indentation [25] as well as with acoustic or vibration methods [29,30]. Further indentation tests where the objective was other than to determine the Young's modulus were conducted [31,32]. Despite the large number of different methods, it can be agreed on an approximate Young's modulus of $E \approx 7.8$ GPa. The elastic constants of lithium single crystals were determined with acoustic techniques [33,34]. The Poisson's ratio was measured to be 0.381 [29]. The yield stress was determined in tensile [19,22,29,35–37] and compression tests [18,21,23]. It is furthermore possible to convert data from hardness tests to yield stresses assuming that $\sigma_y \approx H/3$ [19]. For example the yield stress of lithium at a strain rate of $\dot{\varepsilon} = 5 \times 10^{-3}$ s^{-1} is $\sigma_y = 0.71$ MPa [19]. The creep properties of lithium were studied in tension [29,38] and compression [29,39]. Due to its low melting point, lithium presents significant creep even at room temperature. From the creep experiments and the before mentioned tensile tests, the strain rate dependence was quantified with a stress exponent n between $n = 6.55$ and $n = 6.6$. Despite all these existing studies, some important aspects of the multi-axial plastic behavior, such as the shape of the yield surface, strain hardening and plastic flow, as well as the fracture behavior, were seldom investigated.

The purpose of the present study is to bridge the aforementioned gaps by performing large-deformation tests on pure lithium samples under multi-axial stress states and by characterizing the measured mechanical behavior. Three main challenges could be identified. First, the currently widely-used sample preparation techniques – razor blade and die cutting [19,22,38] – cannot produce complex geometries for multi-axial stress state tests such as tensile tests on central hole specimens. Second, pure lithium has to be handled in a gas-protected environment or in vacuum due to its high reactivity [40]. To avoid the influence of the oxidation by air and humidity, the two procedures of sample preparation and testing are usually performed in the same gas-protected chamber such as an Ar-filled glovebox. However, advanced techniques for the manufacturing of complex-shaped specimens may not be available in a glovebox. Last, pure lithium was reported to be one of the softest metallic materials with the highest ductility, to the best knowledge of the authors. During mechanical tests, severe strain localization (diffuse and localized necking) happens, making the strain measurement extremely difficult. LePage et al.[38] circumvented this problem by designing a tensile specimen with a large-radius notch. In this way, strain localization only occurred in the weakest cross-section so that the authors could focus their cameras for digital image correlation (DIC) on a small range for calculating the local strain. This method came with two limitations. One is that the stress state in the notched sample was no longer ideally uniaxial tensile, particularly when severe necking took place. The other is that the conventional speckle-field-based DIC method with an average speckle size of 0.2mm is usually not reliable enough to process the local strain field when the deformation is extremely large unless a fine speckle field around 0.01mm can be created, for example, using the method by Wang and Wierzbicki [41]. How to make use of fine-speckle techniques without causing oxidation of the pure lithium is another issue to be addressed.

In this study, these three difficulties will be overcome with methods that are different from the aforementioned existing publications. The complex geometry of specimens will be produced by a safe laser cutting technology, the influence of oxidation will be first understood and quantified and then controlled with some simple but effective techniques, and the strain localization problem will be addressed by an inverse method by matching the numerical simulation result to the experimental data.

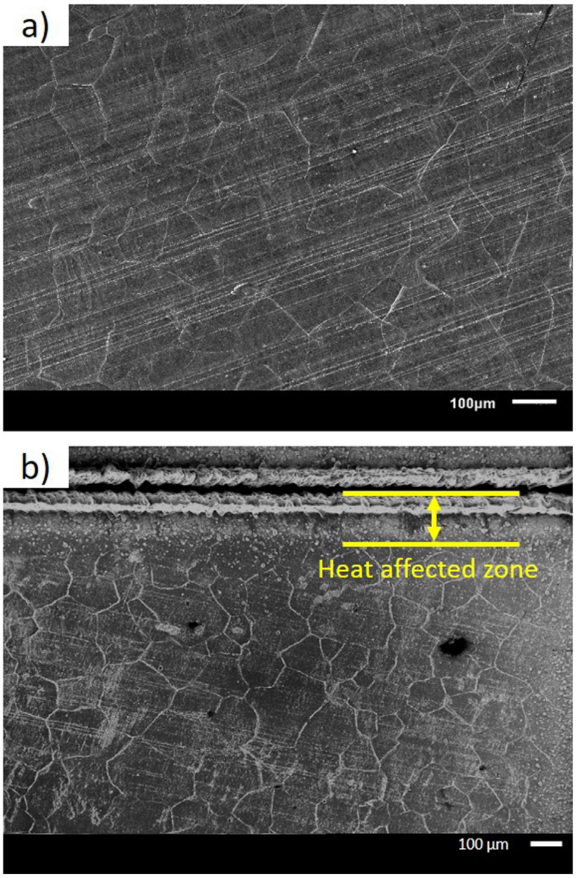

Fig. 1. a) Scanning electron microscope (SEM) image of the microstructure of the as-received Alfa Aesar lithium foil; b) Edge and heat affected zone after laser cutting.

2. Experimental methods

2.1. Material and equipment

Unless otherwise stated, the 750 µm thick battery-grade Alfa Aesar lithium foil (99.9% metals basis, packed in Ar) was used for the experiments. The as-received lithium shows a shiny silver surface with longitudinal grooves due to the rolling process in the manufacturing. The material was extensively studied: it was found to be transversely isotropic in terms of its stress-strain curve and to have a preferential [100] texture in the normal direction to the foil [38]. The microstructure of the as-received foil used for this work is presented in Fig. 1a) and was qualitatively compared to the microstructure of the lithium used by other researchers [19,38]. It was found that the grain size, the grain shape and the surface quality agree with their microstructure. In addition to the qualitative comparison, several SEM graphs taken at different positions of the sample with in total about 500 grains were used for a quantitative grain size analysis. To overcome the influences of the scratches on the sample surface, a cleaning procedure was conducted with software ImageJ to recognize the clear grain boundaries. The identified grains show a clear log-normal grain size distribution. The average grain size was found to be 107 µm with a standard deviation of 49 µm by using the fitting procedure and equations shown in a previous study [42]. It was furthermore noticed that the surface of the as-received lithium was covered with a natural passivation layer. From previous studies it is known that this layer is composed of Li_2CO_3, LiOH and Li_2O [43,44]. The lithium was handled in an Ar-filled glovebox with less than 0.1 ppm water and less than 1ppm oxygen. Unless otherwise stated, all tensile tests were conducted at a displacement rate of $\Delta\dot{l} = 2.4$ mm min^{-1} which corresponds for the uniaxial tension test to a strain rate of $\dot{\varepsilon} = 4 \times 10^{-3}$ s^{-1}. An Instron 5944 universal tensile tester equipped with 100 N load cell, the precision of which was checked for this work, was used.

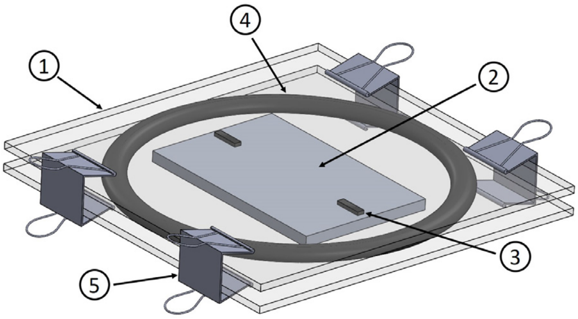

Fig. 2. Argon filled sealed chamber for laser cutting with (1) microscope slide, (2) lithium, (3) spacers, (4) o-ring and (5) binder clip; the laser source is above the assembly.

2.2. Sample preparation by laser cutting

Inspired by the use of the fast, flexible, precise, and highly automatable laser cutting in industrial applications, this technology was chosen to manufacture the tensile specimens. Laser cutting provides a large freedom in geometry and the possibility to make changes in the shape easily. It has already been shown for 50 µm thin lithium foil that laser cutting is possible in dry air and that a risk of fire exists if reaction products on the surface are present [45]. In this work, the method was extended to thicker, more easily commercially available lithium foil and the risk of fire was further minimized by cutting in argon instead of in dry air. A 20 W 1064 nm Electrox Scorpion G2 laser cutter, which for this method is not necessary to be placed in a glovebox, was used. Some of the advantages of laser cutting over the use of a die even for simple geometries are the increased precision of the specimen dimensions and the fact that it is no longer necessary to detach the lithium from the die. All specimens were manufactured parallel to the rolling direction of the foil.

For SEM imaging, a Zeiss Merlin Gemini 2, a Tescan Mira 3 and a JEOL 6610LV were used. The specimens were transferred to the SEM as quickly as possible, resulting in an air exposure of a few seconds. The edge after laser cutting and the heat affected zone are shown in Fig. 1b). The width of the heat affected zone was determined from optical and electron microscope images and was found to be about 150 µm which is much smaller than the specimen dimensions. Furthermore, reference tests with uniaxial tension specimens manufactured with a knife were conducted in order to ensure that the laser cutting does not influence the mechanical properties of the so manufactured specimens. The test results did not show any influence of the heat affected zone, more detail can be found in the Supporting Information. In addition to the small heat affected zone, the edge was found to be of high quality. In the uniaxial tension and the notched tension specimens, fracture initiation was repeatedly observed to be in the center (i.e. on the symmetry axis) of the specimen – not at the edges.

A simple sealed chamber in which the lithium was kept during the cutting process was developed and is shown schematically in Fig. 2. The chamber is composed of two transparent glass microscope slides (1) between which the lithium (2) is placed and fixed in place with two rubber spacers (3). A rubber o-ring (4) is placed around the lithium and the assembly is sealed by applying pressure on the microscope slides with small binder clips (5). By

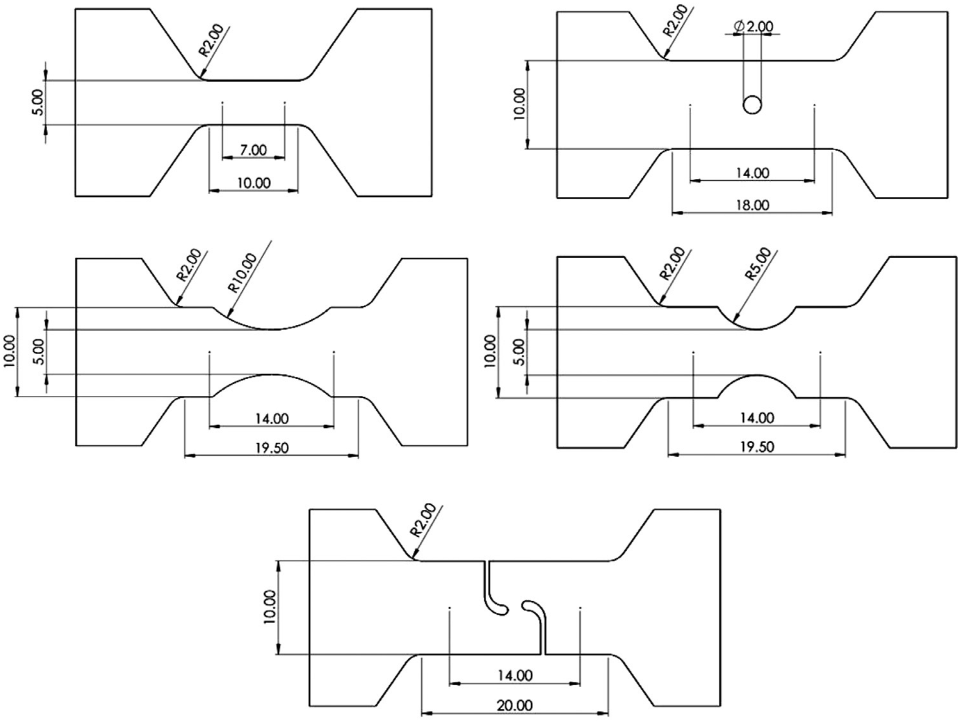

Fig. 3. Specimen geometry for five different stress states, the small points indicate the start and end point of the DIC extensometer. All dimensions are given in mm.

assembling the sealed chamber in a glovebox, the lithium between the two microscope slides is protected by argon even when the assembly is removed from the glovebox. As the glass microscope slides are transparent for the used laser, the whole device can be transferred to a laser cutter, and the lithium can be cut without releasing the seal, thus preserving the protecting argon atmosphere. The rubber spacers (3) have a double function: firstly they fix the lithium foil in place and keep it flat, and secondly they ensure that above the lithium foil some space remains. This space is crucial for a successful cutting because it gives the during the laser cutting evaporated material the possibility to escape from the cutting zone.

To validate the here developed laser cutting procedure, it was performed with lithium foils of two different thicknesses: 370 µm and 750 µm. After the cutting, the sealed chamber could be opened in a glovebox to finish the specimen preparation. It was found that the thin foil could be cut easily and that the specimen detached nearly automatically from the remaining surrounding material, whereas for the thick foil it was necessary to remove the surrounding material manually. Although this was, carefully done, possible and relatively small specimens with a complex geometry could be manufactured, it is recommended to use a thinner foil for smaller specimens or specimens with very complex geometry.

Five different specimen geometries were manufactured in order to conduct tests at five different stress states. The specimen geometry follows closely the geometry of a previously developed set of specimens [46,47] with an overall scaling coefficient of 0.5. The radius of the central hole specimen was chosen as recommended and for the simple shear specimen the geometry recommended for highly ductile materials was used. The final geometry is presented in Fig. 3.

2.3. Testing procedure in argon atmosphere

A glovebox is a very common choice for performing mechanical tests on pure lithium, but it usually comes with much inconvenience in sample installation, test operation, and post-mortem examination. An alternative method was proposed by the authors' team in a previous study [48]. The method consists in conducting the tensile tests in an argon filled Ziploc plastic bag while ensuring that the plastic bag does not influence the result. For this purpose, the specimen is placed into a plastic bag in a glovebox and the plastic bag is sealed. As the plastic bag does not provide a perfect long term protection, the specimen transfer to the tensile tester needs to be done as quickly as possible. The specimen and the plastic bag are clamped together into the tensile tester making sure that the plastic bag can move freely around the specimen. In this way, the plastic bag is not stretched during the tensile test, it “unfolds” without contributing to the stiffness of the specimen. To prevent slip between the clamp, the plastic bag, and the specimen, the clamps need to be closed tightly but carefully to minimize buckling of the specimen. All tests were conducted in a normal lab-environment at room temperature.

A uniaxial tension specimen shortly after fracture initiation is shown in Fig. 4a). It can be observed that the newly formed fracture surface, consisting of pure lithium, remained shiny silver in the argon filled plastic bag which indicates clearly that minimal changes occur from chemical reactions at the time scale of a tensile test. Furthermore, it can be noticed that the specimen appears to be distorted through the plastic bag. Hence, DIC can not be used in combination with the plastic bag method. The testing procedure applied in this work was thus the following: a reference test for which the machine displacement was measured was conducted in a plastic bag. For further tests providing a more accurate displacement measurement, a new specimen was removed from its plastic bag, a speckling pattern was applied on its surface using fast drying color spray and the specimen was immediately tested in air while the displacement was measured both by the tensile tester and by 2D DIC. The average size of the speckles was around 0.2mm. Unless otherwise mentioned, the commercial software VIC-2D was used. The local strain field near the most critical cross-section was also processed for each type of the tests and shown as videos in the Supplementary Information. It can be seen that due

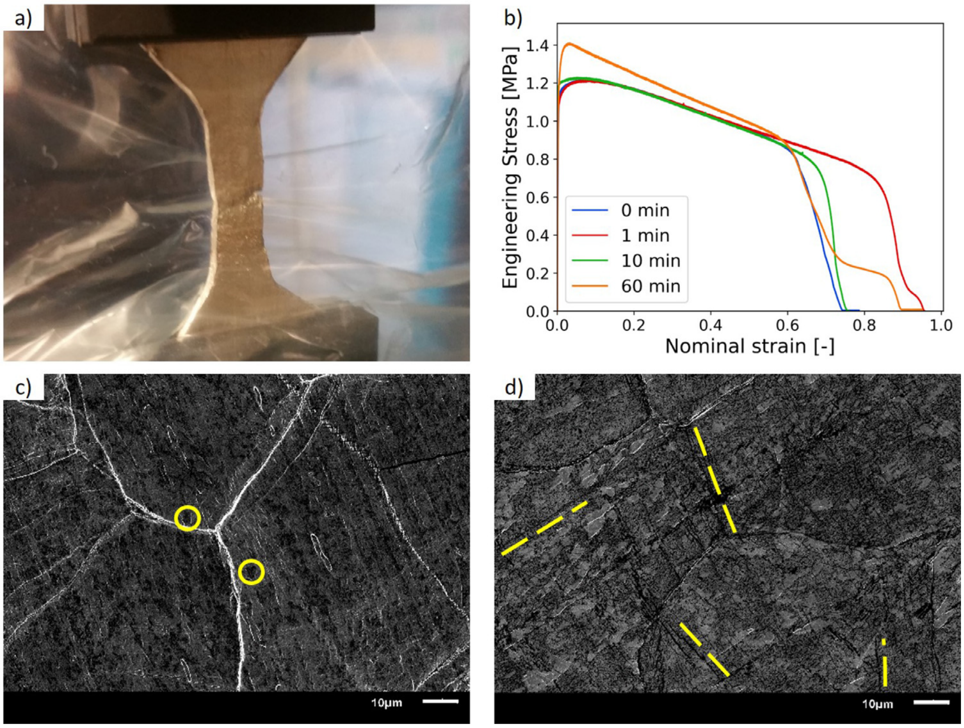

Fig. 4. a) Fracture initiation at a uniaxial tension specimen during a test in an argon filled Ziploc plastic bag; b) Uniaxial tension tests at different times of air exposure before tensile testing; c) Microstructure after a few seconds of air exposure, two isolated particles are exemplary encircled; d) Microstructure after 5min of air exposure, four dashed lines show the beginning network formation.

to the large ductility of pure lithium, the speckle pattern is greatly distorted at the end of the test, and it is difficult to process the local strain from DIC. This observation justifies the motivation of this study of developing a large-deformation plasticity model and obtaining important information of the deformation from numerical simulations.

By comparing the result from the reference test and the specimen which was tested in air, it can be shown that a short exposure to air before and during the test does not influence the result. As shown in Fig. 4b), tests after different time intervals of oxidation have been conducted. The plot shows the nominal strain in the range of the DIC extensometer and the engineering stress. For an oxidation time of 1min and 10min, the difference to the reference test in argon is negligible. After 60min of air exposure, a significant strengthening trend can be observed. Further tests have shown that the results not only depend on the exposure time but also on the atmospheric condition. A short exposition time and dry air have the smallest influence on the mechanical properties of lithium. The plot furthermore shows that the contribution of the plastic bag to the stiffness of the specimen is not measurable: the test corresponding to the curve “0 min” was conducted in a plastic bag whereas the test corresponding to the curve “1 min” was conducted without a plastic bag.

The increased strength of the oxidized specimen can be explained when the microstructure is analyzed. On the surface of a specimen that has been exposed to air for a few seconds during the transfer to the SEM some isolated particles can be observed as it is shown in Fig. 4c). Since these isolated particles merely stick to the surface without being linked to each other, they do not contribute to the stiffness of the specimen and hence do not change the mechanical behavior of the material. From Fig. 4d) it can be seen that with increasing oxidation time, the reaction products start to be linked to each other and form a network that strengthens the specimen. The start of this network formation is highly dependent on the atmosphere and especially on the humidity. Therefore a precise time of air exposure after which this network formation is sufficiently developed to influence the test results can not be determined. Furthermore, a network formation on the sample surface is visible before a change in the stress-strain curve can be observed. This is due to the fact that even though the surface of the sample is beginning to be oxidized, the inner material is not and continues to deliver the mechanical behavior of an unoxidized sample. For longer oxidation times, the number of particles increases until the surface is totally covered by them. After very long air exposure, the originally soft and ductile lithium becomes brittle.

3. Experimental results

3.1. Test results

Each experiment was conducted at least three times with DIC measurements, videos of the tests can be found in the Supporting Information. The results are shown in Fig. 5a)–e). It can be seen that all the four tensile-type tests present a very good repeatability. Only for the simple shear specimen, some fluctuation in the results can be observed which is due to the small size and complex geometry of the specimen. In the force-displacement curves, the displacement was calculated using DIC in the gauge section marked by two points in Fig. 3. With the exception of the simple shear test result, the last plotted point corresponds to the fracture initiation. It was determined by visually choosing the DIC image at which a crack was observed first.

The uniaxial tension test, Fig. 5a), confirms that lithium is an extremely ductile material with early diffuse necking (at a nominal strain around 0.05). The early force maximum is followed by a long monotone plastic deformation with decreasing force. It can be noted that the observed maximum stress of about 1.2 MPa is significantly higher than what is expected from literature values [19,38] (about 0.8 MPa). This is further discussed in Section 5.3. A

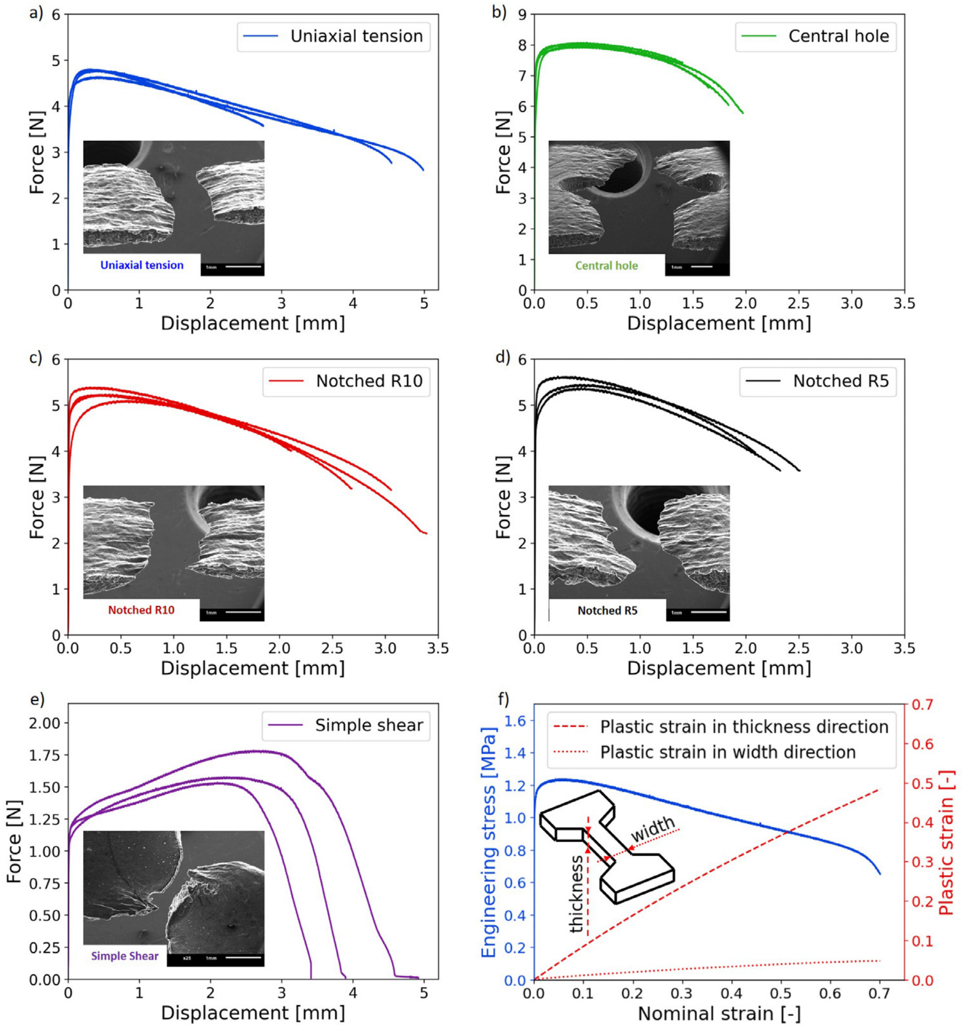

Fig. 5. Force-displacement plots: a) Uniaxial tension specimen; b) Central hole specimen; c) Notched (R10) specimen; d) Notched (R5) specimen; e) Simple shear specimen; f) Measured strain in width direction and calculated strain in thickness direction during the uniaxial tension tests.

nominal fracture strain of about 70% observed. Localized necking can sometimes be observed at multiple locations in a single specimen. A local fracture strain of about 400% has been found using DIC. This value should however be used with caution because of the excessive local deformation of the material and therefore difficult and potentially imprecise DIC measurement.

The fracture displacement decreases when notched specimens are tested and decreases with decreasing notch radius, see Fig. 5c) and Fig. 5d). This can be explained by the increasingly triaxial stress state. While in the case of a uniaxial tension test, the specimen always fails at its weakest point – for example a material imperfection – the notched specimens fracture between the notches. The weakest point in a material sense may not be between the notches, resulting in a higher measured strength.

Since the central hole specimen has a larger gauge width than the uniaxial tension and the notched specimens (8mm in comparison to 5 mm), it is not surprising that the measured force is higher. The central hole being comparable to a notch of 1mm radius, the result further confirms the expectation of a relatively small fracture displacement. The result is displayed in Fig. 5b).

Theoretically, the specimen in the simple shear test should have no change in its thickness and the failure of the specimen should take place through shear bands, as reported by many existing studies on various sheet metals [49,50]. As a result of the absence of thickness reduction, the measured force should keep increasing. This expectation was observed in the simple shear tests of pure lithium – the force did not drop until a large displacement of around 2.5 mm. It is worth noting that this increasing force is a combined effect of three possible effects, which are strain hardening, strain rate strengthening, and the influence of the heat-affected zone due to the small gauge length. At the late stage of the test, due to the large ductility of pure lithium, the stress state becomes a combination of shear and tension, and the tensile portion causes a small amount of necking. Despite the small gauge section (around 1.55 mm) in the shear specimen, a very large fracture displacement can be observed. No fracture initiation or propagation was observed during the shear tests. The plot in Fig. 5e) hence contains data until the complete separation of the two specimen parts.

Although the fracture surfaces for the uniaxial tension, the central hole and the notched specimens show a very similar appearance with significant necking, slight differences can be noticed. In particular for the central hole specimen it can be clearly seen that fracture initiation occurred at the central hole. While the test is continued, the crack slowly propagated to the outer specimen edge until the complete separation of the two parts of the specimen was reached. Lithium shows a perfectly ductile behavior, fracture occurs after localized necking until a specimen thickness of zero is reached, and the two specimen parts separate smoothly without a sharp force drop after slow crack propagation. An exemplary stress

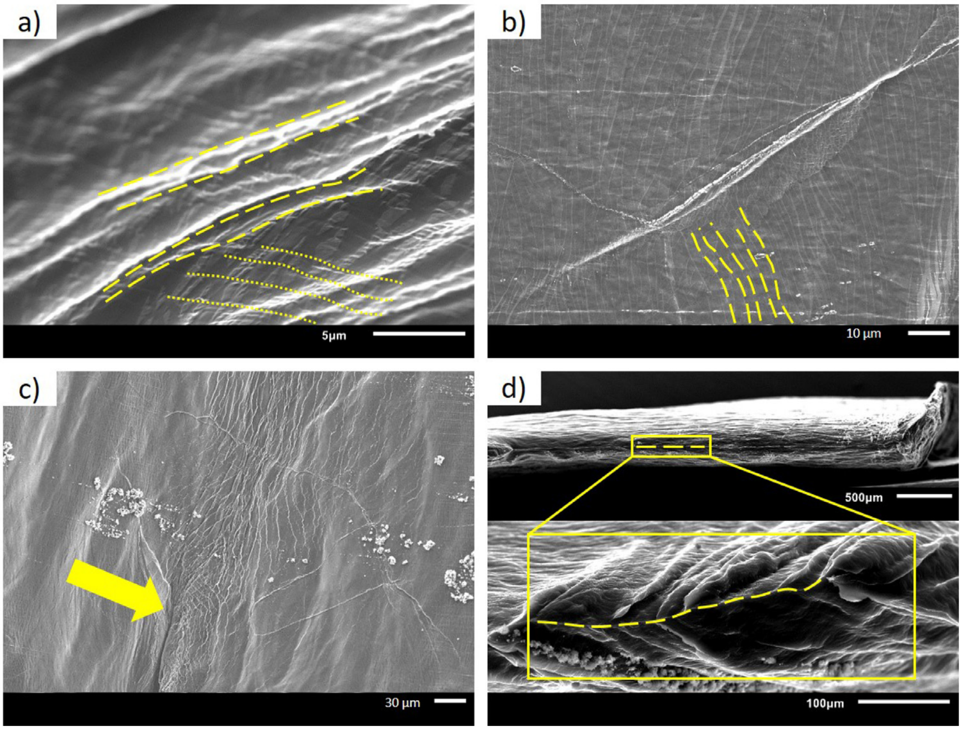

Fig. 6. a) Two active slip systems; b) Wavy slip lines due to cross slip; c) Stress concentration at crack tip, the crack tip is marked with an arrow; d) Fracture surface reduced to a horizontal line and a representative magnified area.

strain curve which also covers the fracture process and shows the smooth force drop can be found in Fig. 4b).

While the above mentioned specimens fracture in a line, the simple shear specimen fractures in a single point. The highly deformed shear section can clearly be seen in Fig. 5e). With ongoing displacement, the two parts of the shear section slide on each other until they are only connected by very little material. From then on, localized necking occurs until the connecting material is reduced to a point.

The above presented results advance the understanding of the fracture behavior of lithium under various stress states. The soft and perfectly ductile fracture behavior is of great importance for battery applications. In contrast to regular graphite anodes that fracture abruptly at a small fracture strain [48,51], the fracture of lithium-metal anodes occurs smoothly at much larger deformations which results in a safer battery behavior when it is deformed.

3.2. Microstructural examinations

The microstructure of lithium was examined before and after deformation. Although the surface of the as-received lithium foil was covered with a thin natural passivation layer, slip lines of the lithium could still be observed since the surface layer followed the movement of the underlying crystal. The slip lines were oriented in different directions in the individual grains and stopped at the grain boundaries. Sometimes, two active slip systems could be observed after deformation as it is shown in Fig. 6a). Moreover, following the large deformation of the lithium, the cracked surface layer could be noticed.

In addition to regular straight slip lines, wavy slip lines were often observed after deformation and can be found in Fig. 6b). These are a result of cross-slip and can also be found in other metals at high temperature [52]. Since the melting point of lithium is low, it is not surprising to observe this phenomenon already at room temperature.

After fracture initiation, a highly deformed area could be observed at the crack tip. This can be seen in Fig. 6c) and is believed to be a combination of stress concentration at the crack tip and the fact that the specimen thickness at this point is extremely small.

In Fig. 6d), a detailed view of the fracture surface is shown. No dimples could be observed on the fracture surface. This can be explained by the high purity of the used lithium, no defects were available for the formation of dimples. Hence, no crack could be initiated, and the whole section deformed and fractured by sliding. The perfectly ductile fracture – with necking until a thickness of zero is reached – can clearly be seen. A straight line in the center of the specimen thickness forms and can be followed from one edge of the specimen to the other. The same fracture can also be observed in other high purity metals [52].

An alternative explanation for the perfectly ductile fracture behavior is the high homologous temperature during the experiments. Lithium is known to fracture in a brittle manner without localized necking at a temperature of 4.2 K [35]. With increasing temperature, lithium shows a ductile fracture behavior with localized necking.

3.3. Anisotropy

The anisotropy of polycrystalline lithium foils has not been sufficiently discussed by the open literature. Many studies treated them as isotropic materials. A recent study by LePage et al. [38] provided a strict validation of this assumption by comparing the stress-strain curves in the rolling direction and transverse direction, which turned out to be identical. Furthermore, the crystallographic texture of the lithium foil was measured by in-plane X-ray diffraction and a preferential crystal orientation was found. However, it shall be pointed out that the through-thickness direction has not been investigated quantitatively. Usually, sheet metals manufactured through rolling such as aluminum alloy and high-strength steels have severe anisotropy [49,53]. Here the anisotropy of the studied lithium foil is investigated by calculating the plastic strain ratio (also known as the Lankford r-value) of the uniaxial tension specimen, which is defined by

$$r = \frac{\varepsilon_w}{\varepsilon_t}, \tag{1}$$

where ε_w is the true plastic width strain and ε_t is the true plastic thickness strain. Based on the assumption that the plastic deformation is isochoric, the alternative formulation

$$r = \frac{-\varepsilon_w}{\varepsilon_w + \varepsilon_l}, \tag{2}$$

where ε_l is the true plastic length strain can be used [54], hence $\varepsilon_t = -(\varepsilon_w + \varepsilon_l)$. The automatic method described in ISO 10113 [54] was applied with a Young's modulus of 7.8 GPa and a Poisson's ratio of 0.381 [29]. Using virtual extensometers on the DIC images that were recorded during the tensile tests, the strain in length and in width direction can be deduced and the strain in thickness direction can be calculated. For this analysis, the softwares Ncorr [55] and Ncorr_post [56] were used.

The results of this analysis are presented in Fig. 5f) which shows a much larger strain in thickness direction than in width direction. At the onset of diffuse necking (maximum of the nominal stress), the plastic strain ratio of the studied lithium foil was found to be $r = 0.138$, which indicates a highly anisotropic deformation behavior. This value confirms that a large strain in the through-thickness direction can be expected during the tensile tests. Since instead of local strain measurements virtual extensometers were used for the calculations, the strain in thickness direction was underestimated. The large strain in thickness direction is experimentally validated through the reduction of the thickness to a line during fracture. The plastic strain value thus provides a coherent explanation of the fracture behavior of lithium in addition to the above mentioned microstructural explanation.

4. Modeling

4.1. Constitutive model

Here the transversely-isotropic form of the quadratic yield function proposed by Hill in 1948 [57] that is being widely used in the metal forming community is adopted,

$$f = \sqrt{F(\sigma_{22}-\sigma_{33})^2 + G(\sigma_{33}-\sigma_{11})^2 + H(\sigma_{11}-\sigma_{22})^2 + 2\,L\sigma_{23}^2 + 2\,M\sigma_{31}^2 + 2\,N\sigma_{12}^2} - \bar{\sigma}_y\left(\bar{\varepsilon}^p, \dot{\bar{\varepsilon}}^p\right) = 0, \tag{3}$$

where F, G, H, L, M, and N are the six parameters to be calibrated, σ_{ij} are the stress components, and $\bar{\sigma}_y$ is the flow stress as a function of the equivalent plastic strain $\bar{\varepsilon}^p$ and its rate $\dot{\bar{\varepsilon}}^p$, also known as the rate-dependent hardening curve. For simplicity, the multiplicative decomposition strategy is used here.

$$\bar{\sigma}_y = \bar{\sigma}_{\mathrm{ref}}(\bar{\varepsilon}^p) f\left(\dot{\bar{\varepsilon}}^p\right), \tag{4}$$

where $\bar{\sigma}_{\mathrm{ref}}$ as a function of just $\bar{\varepsilon}^p$ is the hardening curve under a constant reference strain rate, and f is a function that describes the rate dependence. The measured stress-strain curves suggest that pure lithium is relatively soft and its hardening is not prominent. Therefore the Voce law is used to capture its hardening behavior,

$$\bar{\sigma}_{\mathrm{ref}} = \sigma_0 + (\sigma_{\mathrm{sat}} - \sigma_0)(1 - \exp(-\beta\bar{\varepsilon}^p)), \tag{5}$$

where σ_0 is the first yield stress, σ_{sat} is the saturation stress, and β is the parameter that controls the responding speed to reach saturation.

The rate-dependence of plastic behavior is described by a simple power law

$$f\left(\dot{\bar{\varepsilon}}^p\right) = \left(\frac{\dot{\bar{\varepsilon}}^p}{\dot{\bar{\varepsilon}}^p_{\mathrm{ref}}}\right)^{1/n}, \tag{6}$$

Table 1
Parameters for the Hill48 yield surface of the studied lithium foil.

F (–)	G (–)	H (–)	L (–)	M (–)	N (–)
0.879	0.879	0.121	1.500	1.500	1.992

Table 2
Parameters for the hardening behavior and the strain rate effect of the studied lithium foil.

σ_0 (MPa)	σ_{sat} (MPa)	β (–)	n (–)
1.024	1.389	22.27	6.55

where $\dot{\bar{\varepsilon}}^p_{\mathrm{ref}}$ is the reference plastic strain rate, in this study set at 0.005 s^{-1}. As a result, $\bar{\sigma}_{\mathrm{ref}}$ is the hardening curve obtained under this strain rate.

It is worth noting that the model presented in this study agrees very well with Anand and Narayan [16,17]. The differences lie in three aspects. 1) The hardening law and the rate-dependence power law are both simplified. In Anand model, the hardening is in the rate-form and coupled with rate-dependence. In this model, these two effects are decoupled, in order to make the calibration easier. 2) The through-thickness anisotropy (in the σ_{33} direction) is introduced into the yield function. 3) Here, the additive decomposition of the total strain is used, i.e. $\boldsymbol{\varepsilon} = \boldsymbol{\varepsilon}_{\mathrm{e}} + \boldsymbol{\varepsilon}_{\mathrm{p}}$, while the multiplicative decomposition of the deformation gradient was used in Anand model, i.e. $\mathbf{F} = \mathbf{F}_{\mathrm{e}}\mathbf{F}_{\mathrm{p}}$. From a theoretical point of view, the latter is suitable for modeling large deformation, but the former is also frequently used in metal forming problems and we found that it can also provide satisfactory predictions in this study.

4.2. Calibration and numerical simulations

In total, there are ten unknown parameters in the constitutive model. By neglecting the trivial effects of the shear stresses σ_{13} and σ_{23}, L and M are both assumed to be 1.5, which reduces to the isotropic model. In addition, following the conclusion by LePage et al. [38] about the in-plane isotropy, the model is assumed to be "transverse isotropic". With the measured Lankford r-value of $r = 0.138$, it is determined that $F = G = 0.879$ and $H = 0.121$. In this way, five out of the six parameters in the Hill48 yield function are already determined. The only unknown parameter N describes the possible difference between uniaxial tension σ_{11} and shear σ_{12}. The rate-dependence parameter is obtained from existing publications, $n = 6.55$ [19,38].

To calibrate the remaining four unknown parameters, N, σ_0, σ_{sat}, and β, an inverse method was performed by running simulations of the tests and optimizing the parameters to achieve the best predictions of the force-displacement curves. The details of the inverse method can be found in [49,58,59]. Because uniaxial tension specimens usually come with imperfections on the edge, making it hard to determine the most critical cross-section and predict the necking onset, the other four types of tests (central hole, notched R5, notched R10, and simple shear) were used for the inverse calibration in the present study. A MATLAB code based on the Nelder-Mead Simplex Method was developed for calibration, and the values of all the parameters are listed in Table 1 and Table 2. All the numerical simulations were carried out in Abaqus/Standard with a local mesh size of 75 µm, which guaran-

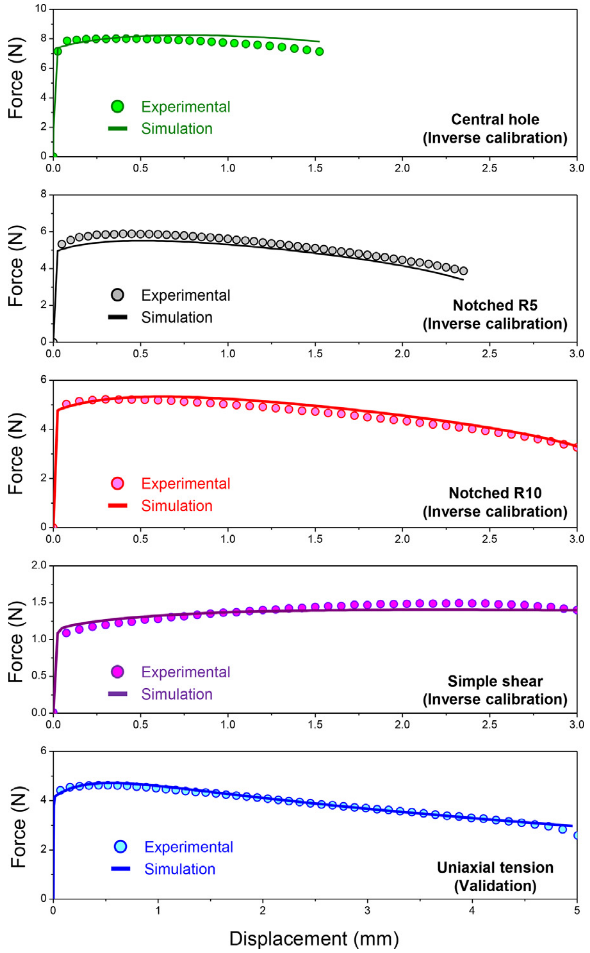

Fig. 7. Simulation results of the five tests. Note that uniaxial tension test has a different scale for the x-axis because of the long elongation.

tees a number of ten elements through the thickness. The displacement rate used in the simulations was taken from the experiments in order to study the effect of the strain rate. After the calibration using the four other tests, the model was applied back to the simulation of uniaxial tension test, as a validation. The simulation results of all the five tests are shown in Fig. 7, where a good agreement between simulations and tests can be observed. Considering that there are five tests that involve multi-axial deformation and that the experimental tests can not perfectly repeat one another either, a small deviation is acceptable.

The initial yield surface is plotted in Fig. 8a) in the space of principal stresses under plane stress condition. For comparison, the isotropic yield surface of von Mises is also plotted. It can be observed that although the lithium foil is transversely isotropic, there is a big difference between its yield surface and the isotropic von Mises, as a result of the anisotropy in the through-thickness direction. A new set of simulations is done using the von Mises yield function with the calibrated hardening curve. The results of the notched R10 test are shown in Fig. 8b). Assuming isotropy clearly results in the over-prediction of the force-displacement response. By introducing anisotropy, the strength in the through-thickness direction is smaller than the in-plane strength. Therefore, the thinning phenomenon is more accurately captured. However, it should be noted that the current simulation can still not perfectly reproduce the experimental observation – the thickness reduction to zero. To improve the prediction of the localized necking behavior, one potentially effective way is to introduce a more advanced form of the hardening curve, for example combining the Voce law with the Swift law [49,58]. One difficulty for the simulation is the computational instability problem caused by the strong localized necking when all the incremental deformation localizes in only one or two elements. Classical necking theories [60,61] can be helpful for modeling this type of perfectly ductile fracture phenomenon. This is a potential continuation of the present study in the near future.

Although all the tests in this study were performed under the same loading speed, considering the rate-dependence in the constitutive model is necessary for numerical simulations. To visualize its effect, a simulation is performed using a rate-independent anisotropic model. The result is also shown in Fig. 8b). The force-displacement prediction turns out to drop rapidly after necking occurs. This is because severe strain localization happens in the test. As a result, the local strain rate can reach as much as over three times of the global averaged strain rate, in all the four tensile tests. In the case of notched tension during localized necking, it is found in the simulations that the deformation are localized in only one row of elements. The local strain rate is thus about ten times of the nominal strain rate calculated by dividing the loading speed with gauge length. Neglecting the rate dependence will not only under-estimate the overall strength but also result in a more severe necking phenomenon. It is found that the thickness reduces to almost zero at a displacement of 0.8 mm, as shown in Fig. 8b), which does not agree with the experimental observation.

From these comparisons, it is clear that the overall plastic deformation is a combined result of small strain hardening, significant rate-strengthening, and strong through-thickness anisotropy. The small strain hardening leads to severe strain localization, resulting in a high local strain rate. The significant rate-strengthening increases the strength of the material in the localization zone, thus preventing localization from developing. These two effects compete with each other, and the overall mechancial behavior of pure lithium is on the equilibrium point of the competition. The strong through-thickness anisotropy causes the more severe thickness reduction than width reduction when subject to tensile loads.

5. Discussion

5.1. Deformation sequence in tensile tests

The deformation sequence of the lithium specimen during simple shear is illustrated in Fig. 9a). Similarly, the deformation and fracture mechanisms for the other tensile tests are shown in Fig. 9b). During deformation, two active slip systems and cross-slip are observed in some grains. The original grains deform excessively until a thickness of zero is reached. In addition to these deformation mechanisms, the strain softening at large deformations can be explained through dynamic recrystallization below the natural passivation layer in the severely deformed grains. Dynamic recrystallization was observed in lithium at room temperature before [40] and is known to lead to a softening effect [62]. Fracture initiation occurs in the center of the specimen. The crack is slowly propagated to the edges of the specimen resulting in a fracture surface in the form of a line. Macroscopically, the phenomenon is a long diffuse necking stage followed by severe localized necking.

5.2. Length scale

In this study, the characteristic length of all the specimens is around 1.5 mm to 5 mm, which is about 10–30 grains. From the point of view of the global deformation, this length scale falls outside the “meso-scale gap” that needs to be bridged. However, with the help of DIC measurement, SEM microstructural examination, as well as numerical simulations, deep insights into the strain localization phenomenon were possible. It was observed that during

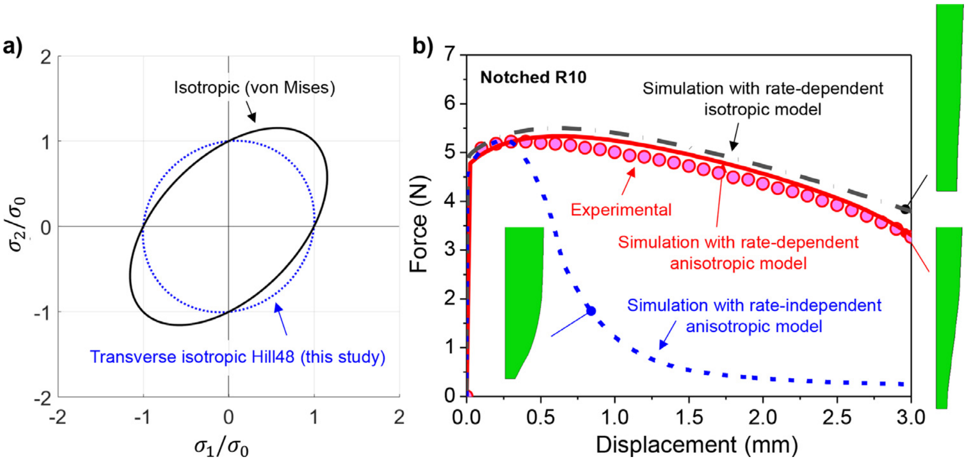

Fig. 8. a) Initial yield surface plotted in the principal stress coordinates (plane stress condition); b) Comparison of notched R10 simulations with different models showing the importance of considering anisotropy and strain-rate dependence.

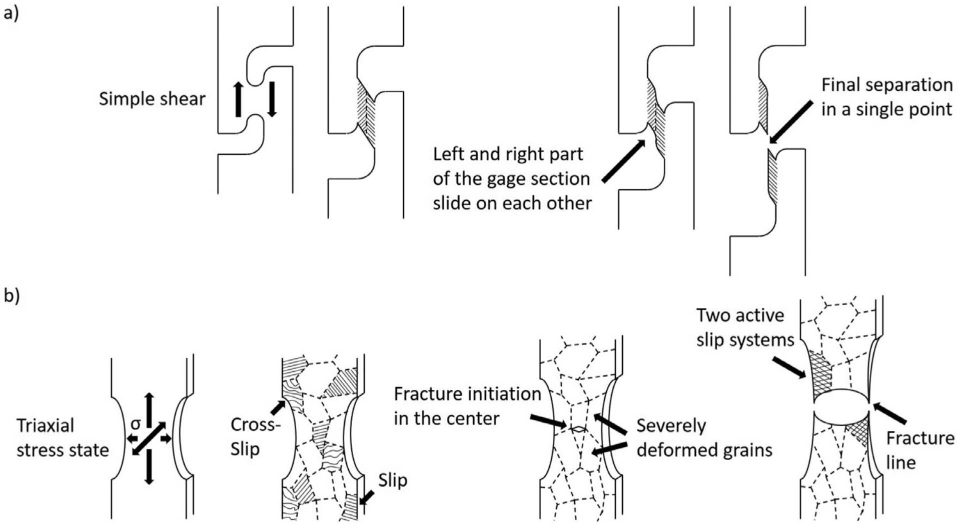

Fig. 9. Graphical summary of the deformation and fracture mechanisms for a) simple shear and b) the remaining tensile tests.

necking, the deformation localizes in several grains. Hence, the investigated length scale is around 150 µm to 1mm, which falls in the meso-scale range.

In order to review the above presented results, a smaller specimen was tested in-situ in an SEM. Two advantages of such a test are that the deformation sequence can be seen clearly and that the specimen is protected from environmental influences during the test. A video of the in-situ test can be found in the Supporting Information and the conclusions that can be drawn from the in-situ test agree very well with the already discussed post-mortem examinations. For example, a wavy surface was clearly observed before fracture and the side view in Fig. 10 shows again that the fracture plane is reduced to a line, which is a clear signal of perfect ductility.

The in-situ tensile test was helpful to understand the deformation sequence, but its further usage for stress analysis was challenged by the precision of the force measurement. Because of the small-sized specimen and the softness of pure lithium, the force was less than 1 N. The use of a conventional load cell resulted in prominent data oscillation. Besides, the long exposition of the specimen to air during the specimen installation in the in-situ tensile tester and the following transfer into the SEM resulted in obvious reaction products especially on the edges of the specimen. Therefore, this type of test did not meet our demand for plasticity modeling.

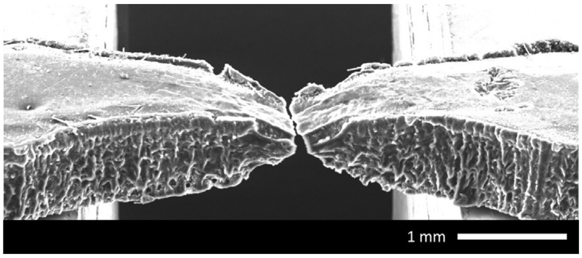

Fig. 10. In-situ notched tension test under SEM: side view of the fracture configuration..

5.3. Comparison with existing data

As already mentioned in Section 3.1, the forces measured in the above described experiments turned out to be larger than what was expected from literature values. After a careful validation of the testing process including a test of the precision of the load cell, the influence of the color spray used to apply the speckling pattern for DIC, the influence of the heat affected zone caused by the laser cutting, and the sealing properties of the plastic bag, it was found that the testing process is not the source of the divergence from literature values. Instead, the material properties of the as-received lithium differ from those of the lithium used by other researchers. The tests were repeated with 370 µm thick lithium foil from MTI Corporation. The result of the uniaxial tensile test coincides with the results in the literature [19,38]. More details can be found in the Supporting Information.

Although the exact reason for the changed material properties remains unclear, an inquiry at Alfa Aesar yielded the result that the lithium used for this work had been supplied from another country than before. It can therefore be concluded that this particular lithium must have received a different treatment by the supplier during the manufacturing leading to changed material properties. Possible reasons include another heat treatment, a changed composition of impurities, a differently composed or thicker natural passivation layer or finally a different preferential orientation of the crystals. A thick passivation layer would also explain why the experiments could be conducted in air: it leads to a reliable long-term protection of the specimen.

5.4. Implications for lithium in battery applications

The contribution of this work is to elucidate the behavior of pure lithium at large deformation and in particular during fracture. This knowledge is of great importance for an improved battery safety. It was found that lithium can resist large deformation and fractures in a perfectly ductile manner without a sharp force drop. Fracture is preceded by significant necking. Therefore, a lithium-metal anode firstly only fractures after very large deformation and secondly does not fracture abruptly. Only from a mechanical point of view, accidentally deformed lithium-metal batteries are thus safer than regular lithium-ion batteries. There is a recent trend of developing flexible batteries where lithium-metal anodes with various manufacturing techniques are considered as a potential candidate. The high ductility of pure lithium makes it promising. However, before that, important mechanical features such as cyclic response, fatigue, and creep should be investigated more deeply.

This work also sheds light on the manufacturing of lithium-metal batteries, particularly on the aforementioned effect of the stack pressure [15]. It is revealed that the tested pure lithium foil has a significant plastic anisotropy in the through-thickness direction – the through-thickness strength is just about 75.4% that in the in-plane direction. When characterizing the stack pressure effect, neglecting this anisotropy will overestimate the strength of the anode and cause error. It is worth noting that the lithium samples in this study were subject to tensile loads during the tests, instead of compression. Polycrystalline sheet metals usually exhibit a degree of tension-compression asymmetry [59]. This asymmetry existing in pure lithium was examined in the experiments of bulk material reported by Masias et al. [29]. However, the degree of asymmetry turned out to be small. It should also be noted that the plastic anisotropy may be changed by the cyclic loads during the charge-discharge operation of the battery. Because this procedure involves complex electro-chemo-mechanical mechanisms including ion transport, reaction, and creeping, it is difficult to draw a conclusion about the trend of the anisotropy change from the current results of the present paper. More experimental data is needed.

The large-deformation plasticity characterization enables the further investigation of the ductile fracture locus of pure lithium at the meso-scale, i.e. the plastic strain at the failure moment as a function of the stress state. Because of the extremely large ductility, it is almost impossible to directly obtain the value of plastic strain from experiments, and a more realistic way is to identify this value from numerical simulations. This type of hybrid experimental-numerical approach has achieved remarkable success on high strength steels and aluminum alloys [46,47,49,58]. However, the accuracy of this approach heavily depends on a high-fidelity characterization of the large-deformation plastic behavior. The present work focused on the diffusive necking stage. To turn the results into a fracture locus, the characterization of the subsequent localized necking stage should be further improved.

6. Conclusion

In order to significantly improve the understanding of the large-deformation mechanisms in pure lithium, a systematic experimental and theoretical study following an established testing method was conducted. The tensile test specimens were manufactured by laser cutting in argon. For this purpose, a simple but effective sealed chamber consisting only of glass microscope slides and a rubber o-ring has been developed. By employing this chamber, the used laser cutter does not need to be placed in a glovebox.

After having proven that a short exposition to air does not affect the mechanical properties of lithium, tensile tests at five different stress states were conducted and the specimens were examined post mortem in an SEM. The deformation mechanisms include cross-slip which results in the observation of wavy slip lines. Furthermore, dynamic recrystallization leads to a significant strain softening during the experiments. Due to the absence of impurities, fracture occurs in a perfectly ductile way after significant necking. No fast crack propagation or dimples were observed at the fracture surface. The highly anisotropic behavior indicated by a low plastic strain ratio is an alternative explanation for the reduction of the specimen thickness to a line.

The lithium foils were modeled as a transversely isotropic material by the Hill48 yield function. The through-thickness anisotropy was described by the Lankford r-value, and the unknown parameters of the model, particularly the hardening law, were obtained through an inverse method by matching the numerical simulation results to the experimental force-displacement curves. At the same time, the rate-dependence was characterized by a power law that was reported in open literature. The prediction of the model agreed very well with the tests. It is found that the overall plastic deformation is a combined result of small strain hardening, significant rate-strengthening, and strong through-thickness anisotropy. There is a competition between the development of strain localization (necking) and the strain rate strengthening of the local necking zone. The present study emphasizes the importance of taking all these three effects into consideration when characterizing the mechanical behavior of pure lithium. It is believed that the data, findings, and model developed in this study will shed light on the development of next-generation batteries.

Declaration of Competing Interest

The authors declare that they have no known competing financial interests or personal relationships that could have appeared to influence the work reported in this paper.

Acknowledgments

T.S., J.Z., J.L., W.L., and T.W. are grateful for the support by AVL, Hyundai, Murata, Tesla, Toyota North America, Volkswagen/Audi/Porsche, and other industrial partners through the MIT Industrial Battery Consortium. Thanks are also due to the MIT-Indonesia Seed Fund to support J.Z.'s postdoctoral study. T.S. would like to thank the Studienstiftung des deutschen Volkes for the visiting student scholarship during his stay at MIT. Further thanks goes to the Photovoltaic Lab at MIT for allowing the use of their laser cutter and to Don Galler and CMSE for helping with the SEM imaging. Thanks are due to Professor Matt Pharr and Mr. Cole D. Fincher for the helpful discussions on comparing lithium foils from different manufacturers. We also thank Professor Lallit Anand and Mr. Sooraj Narayan for providing the Abaqus subroutine code of their lithium model.

Supplementary material

Supplementary material associated with this article can be found, in the online version, at 10.1016/j.actamat.2021.116730

References

[1] B. Liu, J.-G. Zhang, W. Xu, Advancing lithium metal batteries, Joule 2 (2018) 833–845, doi:10.1016/j.joule.2018.03.008.

[2] F. Zheng, M. Kotobuki, S. Song, M.O. Lai, L. Lu, Review on solid electrolytes for all-solid-state lithium-ion batteries, J. Power Sources 389 (2018) 198–213, doi:10.1016/j.jpowsour.2018.04.022.

[3] P. Bai, J. Li, F.R. Brushett, M.Z. Bazant, Transition of lithium growth mechanisms in liquid electrolytes, Energy & Environmental Science 9 (2016) 3221–3229, doi:10.1039/C6EE01674J.

[4] Y. Ren, Y. Shen, Y. Lin, C.W. Nan, Direct observation of lithium dendrites inside garnet-type lithium-ion solid electrolyte, Electrochem. commun. 57 (2015) 27–30, doi:10.1016/j.elecom.2015.05.001.

[5] K. Liu, P. Bai, M.Z. Bazant, C. Wang, J. Li, A soft non-porous separator and its effectiveness in stabilizing Li metal anodes cycling at 10mA cm^2 observed in situ in a capillary cell, Journal of Materials Chemistry A 5 (2017) 4300–4307, doi:10.1039/C7TA00069C.

[6] A. Kushima, K.P. So, C. Su, P. Bai, N. Kuriyama, T. Maebashi, Y. Fujiwara, M.Z. Bazant, J. Li, Liquid cell transmission electron microscopy observation of lithium metal growth and dissolution: root growth, dead lithium and lithium flotsams, Nano Energy 32 (2017) 271–279, doi:10.1016/j.nanoen.2016.12.001.

[7] P. Bai, J. Guo, M. Wang, A. Kushima, L. Su, J. Li, F.R. Brushett, M.Z. Bazant, Interactions between lithium growths and nanoporous ceramic separators, Joule 2 (11) (2018) 2434–2449, doi:10.1016/j.joule.2018.08.018.

[8] Y. Xiao, Y. Wang, S.-H. Bo, J.C. Kim, L.J. Miara, G. Ceder, Understanding interface stability in solid-state batteries, Nature Review Materials 5 (2020) 105–126, doi:10.1038/s41578-019-0157-5.

[9] T. Krauskopf, H. Hartmann, W.G. Zeier, J. Janek, Toward a fundamental understanding of the lithium metal anode in solid-state batteries – an electrochemo-mechanical study on the garnet-type solid electrolyte Li$_{6.25}$Al$_{0.25}$La$_3$Zr$_2$O$_{12}$, ACS Applied Materials & Interfaces 11 (15) (2019) 14463–14477, doi:10.1021/acsami.9b02537.

[10] R. Weber, M. Genovese, A.J. Louli, S. Hames, C. Martin, I.G. Hill, J.R. Dahn, Long cycle life and dendrite-free lithium morphology in anode-free lithium pouch cells enabled by a dual-salt liquid electrolyte, Nat. Energy 4 (2019) 683–689, doi:10.1038/s41560-019-0428-9.

[11] M.J. Wang, R. Choudhury, J. Sakamoto, Characterizing the li-solid-electrolyte interface dynamics as a function of stack pressure and current density, Joule 3 (9) (2019) 2165–2178, doi:10.1016/j.joule.2019.06.017.

[12] C. Monroe, J. Newman, The impact of elastic deformation on deposition kinetics at lithium/polymer interfaces, J. Electrochem. Soc. 152 (2) (2005) 396–404, doi:10.1149/1.1850854.

[13] P. Barai, K. Higa, V. Srinivasan, Impact of external pressure and electrolyte transport properties on lithium dendrite growth, J. Electrochem. Soc. 165 (11) (2018) A2654–A2666, doi:10.1149/2.0651811jes.

[14] X. Zhang, Q.J. Wang, K.L. Harrison, K. Jungjohann, B.L. Boyce, S.A. Roberts, P.M. Attia, S.J. Harris, Rethinking how external pressure can suppress dendrites in lithium metal batteries, J. Electrochem. Soc. 166 (2019) A3639–A3652, doi:10.1149/2.0701914jes.

[15] X. Zhang, Q.J. Wang, K.L. Harrison, S.A. Roberts, S.J. Harris, Pressure-driven interface evolution in solid-state lithium metal batteries, Cell Reports Physical Science 1 (2) (2020) 100012, doi:10.1016/J.XCRP.2019.100012.

[16] L. Anand, S. Narayan, An elastic-viscoplastic model for lithium, J. Electrochem. Soc. 166 (6) (2019) A1092–A1095, doi:10.1149/2.0861906jes.

[17] S. Narayan, L. Anand, A large deformation elastic-viscoplastic model for lithium, Extreme. Mech. Lett. 24 (2018) 21–29, doi:10.1016/j.eml.2018.08.006.

[18] L. Zhang, T. Yang, C. Du, Q. Liu, Y. Tang, J. Zhao, B. Wang, T. Chen, Y. Sun, P. Jia, H. Li, L. Geng, J. Chen, H. Ye, Z. Wang, Y. Li, H. Sun, X. Li, Q. Dai, Y. Tang, Q. Peng, T. Shen, S. Zhang, T. Zhu, J. Huang, Lithium whisker growth and stress generation in an in situ atomic force microscope-environmental transmission electron microscope set-up, Nat. Nanotechnol. 15 (2) (2020) 94–98, doi:10.1038/s41565-019-0604-x.

[19] C.D. Fincher, D. Ojeda, Y. Zhang, G.M. Pharr, M. Pharr, Mechanical properties of metallic lithium: from nano to bulk scales, Acta Mater. 186 (2020) 215–222, doi:10.1016/j.actamat.2019.12.036.

[20] W.D. Nix, H. Gao, Indentation size effects in crystalline materials: A law for strain gradient plasticity, J. Mech. Phys. Solids 46 (3) (1998) 411–425, doi:10.1016/S0022-5096(97)00086-0.

[21] C. Xu, Z. Ahmad, A. Aryanfar, V. Viswanathan, J.R. Greer, Enhanced strength and temperature dependence of mechanical properties of li at small scales and its implications for li metal anodes, Proc. Natl. Acad. Sci. U.S.A. 114 (1) (2017) 57–61, doi:10.1073/pnas.1615733114.

[22] S. Tariq, K. Ammigan, P. Hurh, R. Schultz, P. Liu, J. Shang, Li material testing – fermilab antiproton source lithium collection lens, Proceedings of the 2003 Particle Accelerator Conference (2003).

[23] R. Schultz, Lithium: measurement of Young's modulus and yield strength, Fermilab Technical Memo 2191 (2002).

[24] P.W. Bridgman, The effect of tension on the electrical resistance of certain abnormal metals, Proceedings of the American Academy of Arts and Sciences 57 (3) (1922) 41–66.

[25] Y. Wang, D. Dang, M. Wang, X. Xiao, Y. Cheng, Mechanical behavior of electroplated mossy lithium at room temperature studied by flat punch indentation, Appl. Phys. Lett. 115 (2019) 043903–1–043903–5, doi:10.1063/1.5111150.

[26] Y. He, X. Ren, Y. Xu, M.H. Engelhard, J. Xiao, J. Liu, J.G. Zhang, W. Xu, C. Wang, Origin of lithium whisker formation and growth under stress, Nat. Nanotechnol. 14 (11) (2019) 1042–1047, doi:10.1038/s41565-019-0558-z.

[27] E.G. Herbert, S.A. Hackney, N.J. Dudney, P.S. Phani, Nanoindentation of high-purity vapor deposited lithium films: the elastic modulus, J. Mater. Res. 33 (10) (2018) 1335–1346, doi:10.1557/jmr.2018.83.

[28] C. Campbell, Y.M. Lee, K.Y. Cho, Y. Lee, B. Lee, C. Phatak, S. Hong, Effect of nanopatterning on mechanical properties of lithium anode, Sci. Rep. 8 (2514) (2018), doi:10.1038/s41598-018-20773-8.

[29] A. Masias, N. Felten, R. Garcia-Mendez, J. Wolfenstine, J. Sakamoto, Elastic, plastic, and creep mechanical properties of lithium metal, J. Mater. Sci. 54 (2019) 2585–2600, doi:10.1007/s10853-018-2971-3.

[30] W.M. Robertson, D.J. Montgomery, Elastic modulus of isotoyically-concentrated lithium, Physical Review 117 (2) (1960) 440–442.

[31] Y. Wang, Y. Cheng, A nanoindentation study of the viscoplastic behavior of pure lithium, Scr. Mater. 130 (2017) 191–195, doi:10.1016/j.scriptamat.2016.12.006.

[32] E.G. Herbert, S.A. Hackney, N.J. Dudney, P.S. Phani, Nanoindentation of high-purity vapor deposited lithium films: a mechanistic rationalization of the transition from diffusion to dislocation-mediated flows, J. Mater. Res. 33 (10) (2018) 1361–1368, doi:10.1557/jmr.2018.85.

[33] J. Trivisonno, C.S. Smith, Elastic constants of lithium-magnesium alloys, Acta Metall. 9 (1961) 1064–1071.

[34] T. Slotwinski, J. Trivisonno, Temperature dependence of the elastic constants of single crystal lithium, J. Phys. Chem. Solids 30 (1968) 1276–1278.

[35] D. Hull, H.M. Rosenberg, The deformation of lithium, sodium and potassium at low temperatures: tensile and resistivity experiments, Philos. Mag. 4 (39) (1959) 303–315, doi:10.1080/14786435908233342.

[36] I. Gorgas, P. Herke, G. Schoeck, The plastic behavior of lithium single crystals, Physica Status Solidi A 67 (2) (1981) 617–623.

[37] S. Hori, K. Saito, T. Hasegawa, Plastic workability of pure lithium, Journal of Japan Institute of Light Metals 50 (12) (2000) 660–665.

[38] W.S. LePage, Y. Chen, E. Kazyak, K. Chen, A.J. Sanchez, A. Poli, E.M. Arruda, M.D. Thouless, N.P. Dasgupta, Lithium mechanics: roles of strain rate and temperature and implications for lithium metal batteries, J. Electrochem. Soc. 166 (2) (2019) A89–A97, doi:10.1149/2.0221902jes.

[39] P.M. Sargent, M.F. Ashby, Deformation mechanism maps for alkali metals, Scr. Metall. 18 (1984) 145–150.

[40] M. Krystian, W. Pichl, Metallography of alkali metal single crystals, Mater. Charact. 46 (2001) 1–9.

[41] K. Wang, T. Wierzbicki, Experimental and numerical study on the plane-strain blanking process on an AHSS sheet, Int. J. Fract. 194 (2015) 19–36, doi:10.1007/s10704-015-0034-1.

[42] W. Liu, J. Lian, N. Aravas, S. Münstermann, A strategy for synthetic microstructure generation and crystal plasticity parameter calibration of fine-grain-structured dual-phase steel, Int. J. Plast. 126 (102614) (2020), doi:10.1016/j.ijplas.2019.10.002.

[43] K. Morigaki, A. Ohta, Analysis of the surface of lithium in organic electrolyte by atomic force microscopy, fourier transform infrared spectroscopy and scanning auger electron microscopy, J. Power Sources 76 (1998) 159–166.

[44] X. Xin, K. Ito, A. Dutta, Y. Kubo, Dendrite-free epitaxial growth of lithium metal during charging in Li-O_2 batteries, Angewandte Chemie International Edition 57 (2018) 13206–13210, doi:10.1002/anie.201808154.

[45] T. Jansen, D. Blass, S. Hartwig, K. Dilger, Processing of advanced battery materials – laser cutting of pure lithium metal foils, Batteries 4 (37) (2018), doi:10.3390/batteries4030037.

[46] C.C. Roth, D. Mohr, Ductile fracture experiments with locally proportional loading histories, Int. J. Plast. 79 (2016) 328–354, doi:10.1016/j.ijplas.2015.08.004.

[47] C.C. Roth, D. Mohr, Determining the strain to fracture for simple shear for a wide range of sheet metals, Int. J. Mech. Sci. 149 (2018) 224–240, doi:10.1016/j.ijmecsci.2018.10.007.

[48] Z. Pan, T. Sedlatschek, Y. Xia, State-of-charge dependence of tensile mechanical properties in lithium-ion battery electrodes under different oxidation conditions, J. Electrochem. Soc. 167 (9) (2020), doi:10.1149/1945-7111/ab8804.

[49] J. Zhu, Y. Xia, H. Luo, G. Gu, Q. Zhou, Influence of flow rule and calibration approach on plasticity characterization of DP780 steel sheets using Hill48 model, Int. J. Mech. Sci. 89 (2014) 148–157, doi:10.1016/j.ijmecsci.2014.09.001.

[50] W. Liu, J. Lian, S. Muenstermann, Damage mechanism analysis of a high-strength dual-phase steel sheet with optimized fracture samples for various stress states and loading rates, Eng. Fail. Anal. 106 (2019), doi:10.1016/j.engfailanal.2019.08.004.

[51] J. Lian, T. Wierzbicki, J. Zhu, W. Li, Prediction of shear crack formation of lithium-ion batteries under rod indentation: comparison of seven failure criteria, Eng. Fract. Mech. 217 (2019), doi:10.1016/j.engfracmech.2019.106520.

[52] M. Lederer, V. Gröger, G. Khatibi, B. Weiss, Size dependency of mechanical properties of high purity aluminium foils, Mater. Sci. Eng., A 527 (2010) 590–599, doi:10.1016/j.msea.2009.08.016.

[53] J. Lian, F. Shen, X. Jia, D.-C. Ahn, D.-C. Chae, S. Muenstermann, W. Bleck, An evolving non-associated Hill48 plasticity model accounting for anisotropic hardening and r-value evolution and its application to forming limit prediction, Int. J. Solids Struct. 151 (2018) 20–44, doi:10.1016/j.ijsolstr.2017.04.007.

[54] Metallic materials – sheet and strip – determination of plastic strain ratio, International Standard ISO 10113:2020(E) (2020).

[55] J. Blaber, B. Adair, A. Antoniou, Ncorr: open-source 2d digital image correlation matlab software, Exp. Mech. 55 (6) (2015), doi:10.1007/s11340-015-0009-1.

[56] V. Nežerka, J. Antoš, J. Litoš, P. Tesárek, J. Zeman, An integrated experimental-numerical study of the performance of lime-based mortars in masonry piers under eccentric loading, Constr. Build. Mater. 114 (2016) 913–924, doi:10.1016/j.conbuildmat.2016.04.013.

[57] R. Hill, A theory of the yielding and plastic flow of anisotropic metals, Proceedings of the Royal Society of London. Series A. Mathematical and Physical Sciences 193 (1033) (1948) 281–297, doi:10.1098/rspa.1948.0045.

[58] T. Tancogne-Dejean, M.B. Gorji, K. Pack, C.C. Roth, The third sandia fracture challenge: deterministic and probabilistic modeling of ductile fracture of additively-manufactured material, Int. J. Fract. 218 (2019) 209–229, doi:10.1007/s10704-019-00355-z.

[59] J. Zhu, T. Wierzbicki, K. Pack, S. Roggeband, Characterization of the cyclic loading in the tube expansion process, Int. J. Mech. Sci. 150 (2019) 112–126, doi:10.1016/j.ijmecsci.2014.09.001.

[60] W. Szczepinski, Mechanics of ductile fracture treated as a problem of the theory of plasticity, Int. J. Plast. 6 (1990) 11–27.

[61] E.H. Lee, Plastic flow in a v-notched bar pulled in tension, J. Appl. Mech. 19 (1982) 331.

[62] E. Alabort, D. Putman, R.C. Reed, Superplasticity in Ti-6Al-4V: characterisation, modelling and applications, Acta Mater. 95 (2015) 428–442, doi:10.1016/j.actamat.2015.04.056.